

TOPICAL REVIEW

Fabrication and application of holographic Bragg gratings in lithium niobate channel waveguides

J Hukriede¹, D Runde² and D Kip²

¹ Post str. 29, 49525 Lengerich, Germany

² Technical University of Clausthal, Leibnizstr. 4, 38678 Clausthal-Zellerfeld, Germany

E-mail: hukriede@lycos.de and detlef.kip@tu-clausthal.de

Received 18 December 2002

Published 15 January 2003

Online at stacks.iop.org/JPhysD/36/R1

Abstract

Permanent refractive-index gratings in waveguide devices are of high potential for optical communication systems that make use of the high spectral selectivity of holographic filters, e.g. dense wavelength division multiplexing (DWDM), optical sensors, or narrow-bandwidth mirrors for integrated waveguide lasers. In this contribution we review our results on holographically recorded refractive-index gratings in Cu-doped LiNbO₃ channel waveguides. Elementary holograms are recorded with green light and read in reflection geometry in the insensitive infrared wavelength region around 1.5 μm . To enable long-term stability of the Bragg gratings a thermal fixing technique is applied. In this way strong and almost permanent refractive-index gratings are obtained and their application as narrow-bandwidth filters for DWDM applications is demonstrated. In comparison with Bragg gratings in silica fibres, the electro-optic effect in LiNbO₃ allows for a direct wavelength tuning and a fast, reliable electrical switching of these gratings.

1. Introduction

On the one hand, photorefractive crystals like LiNbO₃, BaTiO₃, KNbO₃, or SBN offer fascinating possibilities in the fields of optical information processing, holographic volume storage, phase conjugation, or interferometric holography. The photorefractive effect in this type of crystals results from a redistribution of charges from impurities or intrinsic centres by means of an inhomogeneous light illumination. Electrons or holes are optically excited and trapped at different sites. In this way a space charge field is build up that modulates the refractive index via the electro-optic effect. For all future devices that are based on these materials, tailored properties like large refractive-index changes, adequate fixing techniques to make gratings permanent, or fast response times during recording are required. Therefore, a detailed knowledge of

the underlying mechanisms of the charge transport and fixing processes is necessary.

On the other hand, especially LiNbO₃ is also a promising substrate material for applications in integrated optics because of its outstanding electro-optical and acousto-optical properties [1, 2]. In this material channel waveguides of high quality can be fabricated by, e.g. indiffusion of thin deposited titanium layers [3] or by proton exchange [4]. By these techniques devices such as directional couplers [5], fast light modulators [6], or complex integrated waveguide lasers [7] have been realized. Most oxide photorefractive crystals are sensitive to light in the visible green or blue wavelength region, but show only little effects in the red or near infrared spectral region. Especially in the 1.3 and 1.55 μm wavelength band of optical communications no light-induced refractive-index changes have been observed in LiNbO₃ at common continuous wave

intensities. In combination with a thermal fixing technique of the refractive-index patterns that makes the gratings insensitive against the erasure with visible light, this allows to design a variety of devices that operate in the infrared wavelength region. Examples are wavelength filters for DWDM, Bragg mirrors for integrated lasers, or optical sensors that make use of the narrow spectral bandwidth of the recorded reflection holograms.

In this contribution, we review our results on holographically recorded refractive-index gratings in titanium indiffused single mode channel waveguides in LiNbO₃ designed for infrared light around 1.55 μm. The samples are additionally diffusion-doped with copper to increase their holographic sensitivity and light-induced refractive-index change. In a first part we derive the theoretical fundamentals of waveguide fabrication and doping by thermal diffusion, introduce the model of holographic recording in the framework of a one-centre model including the technique of thermal fixing, and give an overview on the possibilities for thermal tuning and electrical switching of refractive-index gratings. The section on experimental methods explains the different steps of sample fabrication and the holographic recording and read-out of gratings. The next part describes in detail our experimental results on copper diffusion in LiNbO₃, waveguide properties like surface roughness and optical losses, the photorefractive behaviour of the fabricated samples including the technique of thermal fixing, as well as the fundamental filter properties and electrical switching of the fabricated devices. In a final section, we discuss our results and give a short outlook on further research projects that are currently investigated in our laboratories.

2. Theory

2.1. Refractive-index increase by titanium indiffusion

Within the frame of this work, the coordinate system shown in figure 1 is used. Pieces from *x*- and *y*-cut LiNbO₃ wafers serve as the substrate material for waveguide fabrication. Thin titanium stripes, directed along the *z*-axis of the samples, are created on the top surface by a photolithographic structuring of evaporated layers. The stripes are indiffused into the substrate material by a high temperature annealing process. The presence of titanium ions in LiNbO₃ increases the ordinary and the extraordinary refractive index, thus a waveguide structure is

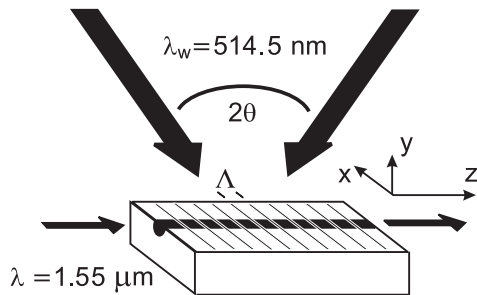


Figure 1. Scheme of the recording and readout geometry for the holographic measurements. The gratings recorded with green light form reflection holograms for the infrared readout light in the channels.

formed. The two-dimensional refractive-index profile depends on the local titanium concentration $c_{Ti}(x, y)$ [15, 16]:

$$c_{Ti}(x, y) = c_0 f(x)g(y), \quad (1)$$

$$c_0 = \frac{2}{\sqrt{\pi} D_y} \tau_{Ti} \rho_{Ti} \operatorname{erf}\left(\frac{W}{2D_x}\right), \quad (2)$$

$$f(x) = \frac{1}{2 \operatorname{erf}(W/2D_x)} \left[\operatorname{erf}\left(\frac{x+W/2}{D_x}\right) - \operatorname{erf}\left(\frac{x-W/2}{D_x}\right) \right], \quad (3)$$

$$g(y) = \exp\left(-\frac{y^2}{D_y^2}\right). \quad (4)$$

Here, τ_{Ti} is the thickness of the evaporated titanium layer, $\rho_{Ti} = 5.64 \times 10^{28} \text{ m}^{-3}$ the density of solid titanium, W the width of the titanium stripe, and D_x, D_y the diffusion depths along the *x* and *y* direction. The diffusion depth D and the diffusion time t are linked with the diffusion constant \mathcal{D} in the following way:

$$D_x = 2\sqrt{\mathcal{D}_x(T)t}, \quad D_y = 2\sqrt{\mathcal{D}_y(T)t}. \quad (5)$$

Here, the diffusion constant depends on the temperature T .

Whereas the extraordinary refractive index n_e increases almost linearly with the titanium concentration c_{Ti} , the ordinary refractive index n_0 shows a strongly nonlinear dependence. The following empirical function well describes the experimental results for the wavelength of a HeNe laser at 632.8 nm [17]:

$$\delta n_{0,632.8 \text{ nm}}(x, y) = \left(\frac{c_{Ti}(x, y)}{F}\right)^\gamma, \quad (6)$$

$$F = 2.9 \times 10^{30} \text{ m}^{-3}, \quad (7)$$

$$\gamma = 0.62. \quad (8)$$

Here, δn_0 is the refractive-index enhancement induced by the presence of titanium. However, this refractive-index increase depends on the wavelength of the probe light. In this work channel waveguides for 1.55 μm are investigated. The dispersion of δn_0 is given by the relation [18]:

$$\delta n_{0,\lambda}(x, y) = \frac{0.67\lambda^2}{\lambda^2 - 0.13} \delta n_{0,632.8 \text{ nm}}(x, y). \quad (9)$$

In this equation, the wavelength λ is taken in microns. For $\lambda = 1.55 \mu\text{m}$ one obtains $\Delta n_{0,1550 \text{ nm}} = 0.71 \Delta n_{0,632.8 \text{ nm}}$. This factor has to be taken into account for the theoretical modelling of channel waveguides.

Finite elements methods are popular tools to calculate the field distributions and effective refractive indices of titanium-indiffused channel waveguides in LiNbO₃. They allow the determination of a characteristic set of fabrication parameters. As a result, low-loss single mode channel waveguides for 1.55 μm are obtained with a width of the titanium stripes of $W = 6\text{--}8 \mu\text{m}$, a thickness of the titanium layer of $\tau_{Ti} = 100 \text{ nm}$, a diffusion temperature of $T = 1000^\circ\text{C}$, and a diffusion time of $t = 18\text{--}22 \text{ h}$.

2.2. Diffusion doping of lithium niobate wafers

In the field of integrated optics commercially available undoped wafers serve as the substrate material for waveguide fabrication. To increase the number of photorefractive centres [19] these wafers can be surface-doped by additional indiffusion of a thin layer of a transition metal, e.g. iron, manganese or copper [20]. Iron is by far the most popular dopant for photorefractive LiNbO₃. However, its main disadvantage compared to copper is the small diffusion constant even at high temperatures.

Diffusion can take place from a depleted or from an undepleted source. For a depleted source the solution of Fick's laws is a Gaussian function:

$$c(y) = c_0 \exp\left(-\frac{y^2}{D_y^2}\right), \quad (10)$$

$$c_0 = \frac{2}{\sqrt{\pi} D_y} \tau \rho. \quad (11)$$

In this equation, $c(y)$ is the concentration of the metal in the substrate material, D_y the diffusion depth, τ the thickness of the evaporated layer, and ρ the atomic density of the evaporated material.

If the diffusion time is too short a fraction of the evaporated material still remains on the surface of the crystal. This means that the diffusion source is not depleted yet. Now diffusion from an undepleted source takes place and the solution of Fick's laws follows the complementary error function:

$$c(y) \sim \operatorname{erfc}\left(-\frac{y}{D_y}\right). \quad (12)$$

Diffusion doping of channel waveguides requires an almost constant impurity distribution over the cross section of the channel waveguide and a complete indiffusion of the evaporated material. This can be obtained by properly adjusting the diffusion time at a given temperature.

2.3. Hologram formation and one-centre model of charge transport

The 'one-centre model' [21] was developed to describe the process of hologram recording in iron-doped LiNbO₃ crystals. It was also successfully transferred to LiNbO₃-doped with copper [11]. Copper appears in two different valence states in the crystal, Cu⁺ and Cu²⁺. Illumination with a light intensity pattern in the green or blue wavelength region excites electrons in the bright regions from Cu⁺ ions which act as filled traps. The charge carriers are redistributed in the sample and finally trapped in the dark regions at Cu²⁺ sites. The bulk photovoltaic effect is the main charge driving force [22]. In LiNbO₃ the light-induced redistribution of charges generates a space charge field which modulates the refractive index of the material via the linear electro-optic effect.

The one-centre model predicts several linear relations between the concentrations of filled and empty traps, c_{Cu^+} and $c_{\text{Cu}^{2+}}$, if sufficient traps are present. Important results are $\sigma_{\text{ph}} \propto (c_{\text{Cu}^+}/c_{\text{Cu}^{2+}})I$, $\Delta n_s \propto c_{\text{Cu}^{2+}}$, and $j_{\text{phv}} \propto c_{\text{Cu}^+}$. Here, σ_{ph} is the photoconductivity, I the light intensity in the crystal,

Δn_s the saturation value of the light-induced refractive-index modulation, and j_{phv} the bulk photovoltaic current.

Furthermore, the build-up of the light-induced refractive-index change Δn during hologram recording and its decay under homogeneous illumination follow exponential laws:

$$\text{Recording: } \Delta n(t) = \Delta n_s \left(1 - \exp\left(-\frac{t}{\tau}\right)\right), \quad (13)$$

$$\text{Erasure: } \Delta n(t) = \Delta n_0 \exp\left(-\frac{t}{\tau}\right), \quad (14)$$

$$\tau = \frac{\epsilon \epsilon_0}{\sigma_{\text{ph}}}. \quad (15)$$

Here, t is the time, $\epsilon = 28$ is the appropriate dielectric constant of LiNbO₃ [23], and ϵ_0 is the permittivity of free space.

Elementary holograms are recorded by superimposing two coherent plane waves on the sample. The generated sinusoidal light intensity pattern is transferred into a sinusoidal modulation of the refractive index of the crystal. A Bragg grating is formed which allows to diffract light beams in transmission or reflection geometry. The diffraction efficiency η of an unslanted reflection grating depends on Δn and the wavelength λ of the read out beam via the relation [24]:

$$\eta = \left(1 + \frac{1 - \chi^2/\Phi^2}{\sinh^2(\Phi\sqrt{1 - \chi^2/\Phi^2})}\right)^{-1}, \quad (16)$$

$$\Phi = \frac{\pi \Delta n d}{\lambda}, \quad \chi = \frac{(\lambda - \lambda_p)\pi d}{\lambda_p \Lambda}. \quad (17)$$

Here, d is the thickness of the Bragg grating, Λ the grating period, and λ_p the peak wavelength where the Bragg condition is exactly matched. For $\lambda = \lambda_p$ equation (16) simplifies to

$$\eta = \tanh^2\left(\frac{\pi \Delta n d}{\lambda_p}\right). \quad (18)$$

The peak wavelength λ_p of the grating is given by the grating period Λ :

$$\lambda_p = 2n\Lambda. \quad (19)$$

Here, n is the refractive index of the material at the wavelength of the read out beam. If single mode channel waveguides are used for readout, the effective refractive index n_{eff} of the guided mode has to be used.

The period Λ of a Bragg grating in a photorefractive crystal is given by the intersecting angle 2Θ of the two recording beams that form the interference pattern:

$$\Lambda = \frac{\lambda_w}{2 \sin \Theta}. \quad (20)$$

In this equation λ_w is the wavelength of the writing beams.

2.4. Thermal fixing

A hologram recorded at room temperature in photorefractive LiNbO₃ has only a limited lifetime. There are two main effects that shorten the lifetime of the hologram: first, the Bragg grating in the crystal is not stable against further illumination with green or blue light. Charge carriers are redistributed again via the bulk photovoltaic effect which leads to the erasure of

the original space charge field and the Bragg grating. Second, LiNbO₃ crystals show a non-negligible dark conductivity. Even when the sample is not illuminated, charge carriers slowly move in the material and tend to screen the light-induced space charge field. This leads again to the erasure of a previously recorded Bragg grating.

A popular method to stabilize a recorded hologram in doped LiNbO₃ versus the read out light is the technique of thermal fixing [25–27]. Thermal fixing has been investigated intensively in iron-doped volume crystals, and the process is now well understood for this dopant. During or after hologram recording the crystal is heated to elevated temperatures around 180°C. In this temperature range, the mobility of protons, which are incorporated into the material already during the crystal growth, becomes considerably large. When a hologram is recorded while heating the crystal, the protons permanently compensate the light-induced space charge field. As a result, the redistribution of electrons between Fe²⁺ and Fe³⁺ sites is not limited anymore, causing a strong modulation of the Fe²⁺ ions. After switching off the recording beams the sample is cooled down to room temperature and the protons become nearly immobile. They now stabilize the strong modulation of the Fe²⁺ ions. In a last step a homogeneous development process with incoherent photoactive light is applied. The bulk photovoltaic effect now generates modulated photocurrents resulting from the modulated Fe²⁺ concentration. As a result, a space charge field builds up and the thermally fixed hologram appears.

The fixed hologram is insensitive against further illumination: if light shines on the crystal it helps to develop the hologram but does not erase it anymore. Erasure can only be achieved by heating up the sample to elevated temperatures. Furthermore, if the developed space charge field is slowly erased via the dark conductivity, a new development process can be applied to ‘refresh’ the hologram. However, this is a crucial disadvantage in applications like thermally fixed narrow bandwidth filters in LiNbO₃ [28–30] that are designed to work permanently for many years. It also makes it impossible to fabricate passive components with LiNbO₃:Fe because a light source is required from time to time for a new development process. This is our motivation to investigate copper doping in LiNbO₃ as an alternative.

2.5. Electrical tuning of Bragg gratings via the electro-optic effect

The refractive index n of an electro-optic crystal can be changed by applying an external electric field E . When channel waveguides are used, the effective refractive index n_{eff} replaces n :

$$\Delta n_{\text{eff}} = -\frac{1}{2}n_{\text{eff}}^3 r_{ijk} E_k. \quad (21)$$

Here, r_{ijk} is the appropriate element of the linear electro-optic tensor and E_k the corresponding component of the electric field. Replacing Δn_{eff} by $(\partial n / \partial \lambda) \Delta \lambda$ and making use of equation (19) leads to a relation for the linear electro-optic coefficient:

$$r_{ijk} = \frac{\Delta \lambda}{n_{\text{eff}}^3 E_k \Lambda}. \quad (22)$$

On the one hand, this allows us to calculate the value of the involved electro-optic coefficient by measuring the shift of the centre wavelength of a Bragg grating when an external electric field is applied. On the other hand, the peak wavelength of a Bragg grating can be electrically tuned, allowing for example for fast electrically switchable filters for DWDM applications.

3. Experimental methods

3.1. Diffusion constant of copper in lithium niobate

To determine the diffusion constant of Cu in LiNbO₃, an undoped polished y -cut LiNbO₃ wafer of the congruently melting composition (from Crystal Technology) is cut into pieces of $8 \times 10 \text{ mm}^2$. The c -axis of the crystal is pointing along the 10 mm-side and the thickness y_0 of each sample is 1 mm. A 500 nm-thin layer of copper is deposited by thermal evaporation on the top face of the crystal. Then the layer is successively indiffused into the substrate at a temperature of 1000°C in air. From time to time, the sample is cooled down and the c -face (oriented rectangular to the top face) is precisely polished to optical quality. This face is scanned along the y -direction by the focused electron beam of an electron microprobe (focus diameter $< 1 \mu\text{m}$, acceleration voltage 25 keV) to determine the distribution of copper atoms in the sample. As a reference, the signals of oxygen and niobium atoms are also monitored simultaneously. The step width of the electron beam is $\delta y = 1 \mu\text{m}$. After 1000 steps the whole sample is scanned and the copper indiffusion is carried on with the next annealing step. Fit curves to the data according to equations (10) and (12) yield the diffusion constant D_{Cu} .

3.2. Fabrication of channel waveguides

Undoped and polished x - and y -cut LiNbO₃ wafers are cut into pieces of $7 \times 17 \text{ mm}^2$, where the c -axis of the crystals points along the 17 mm-side. By electron beam evaporation a 100 nm-thick film of titanium is deposited on the top face of each sample. With the help of photolithography followed by a wet chemical etching process arrays of titanium stripes are fabricated on the various substrates. Each set contains channels from 4 to 10 μm width. The stripes are directed along the c -axis of the crystals. Next, a high temperature indiffusion of the titanium at 1000°C in air is applied creating single mode channel waveguides for infrared light around 1.55 μm . Here, the diffusion time is 20 h. During annealing the samples are wrapped in platinum foil. After cooling down, thin copper layers of various thicknesses τ_{Cu} are deposited on the top face of the samples by thermal evaporation. The layers are indiffused utilizing a second short annealing treatment at a temperature of 1000°C. This increases the number of photorefractive centres in the channels. The number of Cu⁺ and Cu²⁺ centres is influenced by the diffusion atmosphere: compared to a diffusion in air, a diffusion in argon environment increases the number of Cu⁺ traps. In contrast, a diffusion in oxygen atmosphere increases the number of Cu²⁺ sites.

With the help of the diffusion constants of copper [31] and titanium [32] in LiNbO₃ at 1000°C, which are determined with the method described above, the concentration profiles of the metals in the samples along the y -direction are calculated. Figure 2 shows the result for an 8 μm -wide channel in the

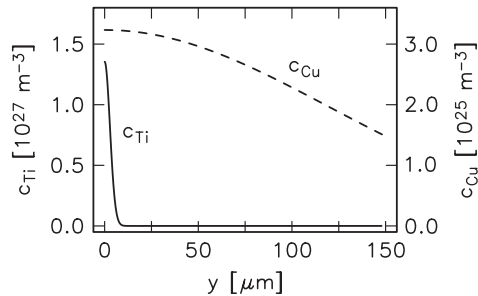


Figure 2. Calculated titanium and copper concentrations c_{Ti} and c_{Cu} versus crystal depth y for the waveguide ‘K4’ (57 nm Cu) in the centre of the $8 \mu\text{m}$ -wide channel. The copper concentration is almost constant in the waveguide layer.

Table 1. Summary of the main fabrication parameters of the waveguides.

Sample	τ_{Cu} (nm)	t (h)	c_{Cu} (10^{25} m^{-3})	ox/red	l (mm)
U3	—	—	—	—	16.0
K1	6	2	0.4	red	15.0
K3	19	2	1.1	red	14.0
S2	19	2	1.1	red	15.0
K5	38	2	2.2	red	15.0
V2	38	2	2.2	red	3.0
K4	57	2	3.2	red	16.0
S3	57	2	3.2	red	15.0
S4, S5, S6	83	2	4.7	red	16.0
T4	51	0.5	5.7	red	16.3
X1-5	83	2	4.7	red	16.0
W3	38	2	2.2	ox	15.6
W2	38	2	2.2	st. red	16.0

Here, τ_{Cu} is the thickness of the evaporated copper layer, t the copper diffusion time, c_{Cu} the copper concentration in the channels and l the length of the copper doped region of the waveguide. ‘red’: Copper was indiffused in reducing environment (argon atmosphere), ‘st. red’: strongly reduced, copper was indiffused in vacuum atmosphere, ‘ox’: copper was indiffused in oxidizing environment (oxygen atmosphere). All samples are fabricated on y -cut substrates, except for the sample X1-5 (x -cut).

waveguide ‘K4’ (57 nm Cu). Here, the distribution $c_{\text{Ti}}(x = 0, y)$ of titanium (calculated for the centre of the channel) is a measure for the depth of the waveguide. As a result of the strongly different diffusion constants the copper doping level in the channel is nearly constant. On the first $10 \mu\text{m}$ (measured from the sample surface) it varies less than 0.5%. In the following, the term c_{Cu} always refers to the calculated copper concentration in the channel. The fabrication parameters of the investigated channel waveguides are summarized in table 1.

The reduction state of the copper ions in homogeneously doped LiNbO_3 volume crystals can be measured easily by absorption spectroscopy. Cu^+ produces a pronounced absorption shoulder around 380 nm, whereas Cu^{2+} generates an absorption band around 1100 nm [11]. The broad Cu^+ absorption is often detected with a probe beam at 477 nm. Both absorption values are proportional to the concentration of the involved copper ion. For diffusion doped channel waveguides, this method of analysis cannot be applied: the copper distribution along the y -direction is inhomogeneous. Also, the presence of a large amount of titanium ions in the channels might influence the reduction state of the copper ions

and the number of Cu^+ traps can be different compared to the substrate material. Consequently, we cannot present data on the reduction state of the copper in the fabricated waveguides.

After the annealing treatments are finished the endfaces of the waveguides are precisely polished to optical quality to allow for the coupling of light. In a final step, each waveguide endface is anti-reflection coated with a single layer of 290 nm MgF_2 . This material can be deposited while the sample is kept at room temperature in the evaporation chamber, thus preventing an undesired change of the reduction state of the copper during the coating process. The bottom faces of the samples are anti-reflection coated for the green recording light with a single layer of 110 nm MgF_2 .

Some experiments with external electric fields applied to the samples are performed in this work. For this purpose, planar parallel silver electrodes are fabricated on both sides of the channel waveguides. The distance between the electrodes of $d_e = 58 \mu\text{m}$ is verified under a microscope. The strength of the electric field in the channel can be calculated from the applied voltage U and the electrode distance d_e :

$$E = \frac{U}{\pi d_e}. \quad (23)$$

3.3. Holographic recording setup

Refractive-index gratings are recorded in the samples with the help of a two-beam holographic setup utilizing an active phase stabilization system [33]. This avoids phase changes between the two writing beams during the recording process which would result in an undesired movement of the light interference pattern on the waveguide. This is critical especially for high temperature recording experiments. The recording and read-out geometry is illustrated in figure 1. Green light from an argon ion laser at a wavelength of $\lambda_w = 514.5 \text{ nm}$ is split into two coherent, ordinarily polarized beams. The first beam (1) is spatially filtered, expanded and impinges onto the sample as a plane wave. The second beam (2) is coupled into a polarization preserving single mode fibre. The fibre output collimator is mounted onto a precise rotary table together with a collimating system. The expanded beam also hits the sample and a light interference pattern is formed on the top face of the waveguide. The light intensity of each recording beam is 600 W m^{-2} . The angle 2Θ between the two recording beams is precisely adjusted by moving the rotary table that holds the collimating system. The symmetric position of the sample is adjusted by auto collimation: beam (2) is blocked before the light enters the optical fibre. Beam (1) is switched on and the sample is adjusted carefully until the light reflected from the crystal surface travels exactly through the optical fibre in the opposite direction. This makes sure that the surface normal of the sample is perfectly aligned in the plane of the recording beams, and in the symmetric position. In this way, the grating vector is exactly directed along the z -direction of the crystal, parallel to the channels on top of the sample. The angle mismatch between grating vector and channel in the xz -plane is less than 0.3° . Besides the period that is given by equation (20) the length of the grating strongly influences its filter shape. Different grating lengths are realized experimentally by applying an appropriate slit on top of the sample during hologram recording.

Thermal fixing of holographic gratings is performed in the following way: the waveguide is placed on a heatable mount and kept at a temperature of 180°C with the help of a temperature controller. The crystal temperature is measured with a PT100 sensor that is mounted close to the sample. After about 30 min, the temperature of the crystal is stable to within $\pm 0.1^\circ\text{C}$. Now the recording beams are switched on and the grating is recorded. After shutting down the writing beams the sample is cooled down rapidly to room temperature. It reaches 20°C within 5 min. At room temperature, a development process can be applied. This is done with an expanded beam of the argon ion laser (intensity 170 W m^{-2}) or, alternatively, with a 150 W halogen lamp equipped with a goose neck. An illumination time of 30 min with the halogen lamp at full power is sufficient to reach saturation.

3.4. Setup for endface coupling

All waveguides are investigated with infrared probe light supplied by a DFB laser (Profile PRO800) equipped with an optical fibre output. The DWDM test system is tunable between 1555.40 and 1559.40 nm in steps of 0.01 nm and has a line width smaller than 1×10^{-4} nm. The light is directed through an optical fibre isolator to eliminate back reflections that might enter the laser output. A 2×2 -coupler (splitting ratio 50%) is appended which allows to permanently monitor the emitted laser power. Finally, an adjustable fibre polarizer is inserted to control the polarization state of the infrared light. This allows to excite either the TE or the TM mode in the channel waveguide. The light is coupled in and out of the investigated channel by direct fibre-to-channel coupling via the polished endfaces of the samples. For this purpose, the bare fibre ends are mounted on precise piezo-driven xyz -translation stages allowing to adjust the fibre positions with an absolute accuracy better than 30 nm. The outcoupled light is directed on a germanium photo detector with the help of a second optical fibre.

The loss of light intensity during coupling from the single mode fibre into the channel is estimated in the following way: the overlap integral ρ between the field distribution F_f in the fibre and the field F_{ch} in the channel is calculated numerically via the formula

$$\rho = \frac{|\iint F_f F_{ch} dx dy|^2}{\iint |F_{ch}|^2 dx dy \times \iint |F_f|^2 dx dy}. \quad (24)$$

Here, F_{ch} is calculated from the refractive-index profile of the channel waveguide with the help of a finite differences method. For the prepared waveguides a value of typically $\rho = 90\%$ is obtained. Fresnel reflections of about 4% occur at the transition between fibre and air because the fibres are not coated. To take into account imperfect polishing and cleaning of the endfaces of waveguide and fibre an additional loss of 5% is assumed. All in all, approximately 18% of light intensity gets lost at the transition from fibre to channel. The losses α in the channel itself are calculated according to the relation $\alpha = -1/l \times \ln(I_{out}/I_{in})$ where l is the length of the waveguide, I_{in} the light intensity at $z = 0$ and I_{out} the intensity at $z = l$.

The recorded Bragg gratings are read in reflection geometry in the channels by tuning the wavelength of the DFB laser in steps of 0.01 nm and measuring the normalized

transmission $T(\lambda)$ of the channel. At the peak wavelength λ_p the Bragg condition for readout is exactly matched, according to equation (19). The transmission $T(\lambda)$ drops down from its initial value of 1 to a minimum. The diffraction efficiency of the holographic grating is given by $\eta = 1 - T(\lambda_p)$.

The photoconductivity σ_{ph} in the channels is evaluated by measuring the decay under homogeneous illumination of a holographic grating recorded at room temperature. Transmission spectra $T(\lambda)$ are taken at defined time intervals while an expanded green beam of the argon ion laser impinges on the top face of the waveguide.

The time evolution of the development process of thermally fixed gratings, and also the erasure process of room temperature gratings, is measured in the read out setup as well: the sample is placed in the mount and is homogeneously illuminated with green light. In this measurement, the light intensity is about 250 W m^{-2} . During illumination the evolution of η is measured by taking transmission spectra with the DFB laser. The dark compensation of a developed grating is monitored by taking transmission spectra from time to time while the sample is kept in the dark. In this way, the weak infrared readout light (power about $100\ \mu\text{W}$) does not affect the time evolution of η .

The effective refractive indices n_{eff} of the channel waveguides are measured by recording a reflection grating and extracting the resulting peak wavelength λ_p for the infrared light. By combining equations (19) and (20) one obtains a relation for the effective refractive index: $n_{eff} = \lambda_p \sin(\Theta)/\lambda_w$. Further details regarding the waveguide fabrication and the recording and readout setup can be found in a previous work [34].

4. Experimental results

4.1. Copper diffusion into lithium niobate

Figure 3 shows the measured copper distribution in the test sample after a total diffusion time of $t = 1\text{ h}$. After this short time interval the evaporated copper has not indiffused completely into the sample yet, and a thin layer of material remains on the surface of the crystal. This results in an additional sharp peak appearing at $y = 0$ during the microprobe scan, indicating that up to now diffusion from an

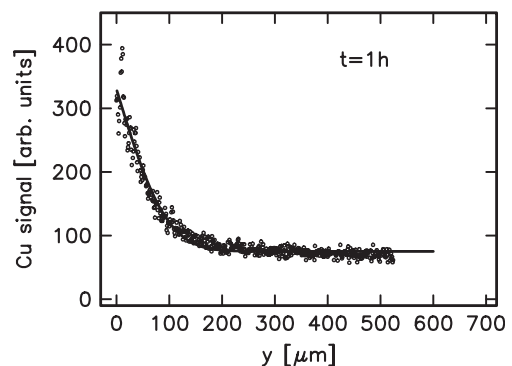


Figure 3. Copper signal (symbols) detected with an electron microprobe versus material depth y after a total annealing time of 1 h. The solid line is the best fit yielding the corresponding penetration depth ρ .

undepleted source has taken place. After manually removing the surface peak from the measured copper signal the curve is well described by equation (12) if a constant value c_{Cu}^0 is added to take into account the constant signal background. The solid line indicates the best fitting curve. In figure 4, the same measurement after a total diffusion time of $t = 7$ h is presented. Here, the copper signal from the remaining layer has just vanished but the curve is still well described by equation (12). Diffusion from a depleted source would result in a Gaussian shaped curve. However, it does not describe the measured data very well. Figure 5 presents the square of the extracted diffusion lengths D_y^2 versus the quadruple diffusion time $4t$. According to equation (5) a linear fit yields the corresponding diffusion constant \mathcal{D}_y . For copper diffusion into LiNbO₃ along the y -axis at 1000°C the following value is derived [31]:

$$\mathcal{D}_{\text{Cu},y} = (1.0 \pm 0.2) \mu\text{m}^2 \text{s}^{-1}.$$

This is more than 500 times higher than the diffusion constant of iron under the same conditions that has been measured in a previous work: $\mathcal{D}_{\text{Fe},y} = (1.8 \pm 0.2) \times 10^{-3} \mu\text{m}^2 \text{s}^{-1}$ [32]. We also determined the diffusion constant of manganese ($\mathcal{D}_{\text{Mn},y} = (7 \pm 1) \times 10^{-3} \mu\text{m}^2 \text{s}^{-1}$) and titanium ($\mathcal{D}_{\text{Ti},y} = 4.4 \times 10^{-5} \mu\text{m}^2 \text{s}^{-1}$) in y -cut LiNbO₃ under the same conditions [32]. The diffusion constant of copper is large enough to produce surface-doped waveguide substrates

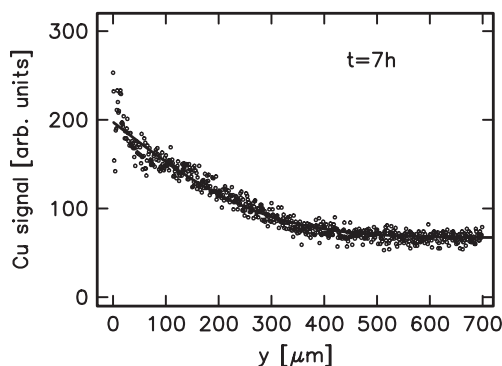


Figure 4. Copper signal (symbols) detected with an electron microprobe versus material depth y after a total annealing time of 7 h. The solid line is the best fit yielding the corresponding penetration depth ρ .

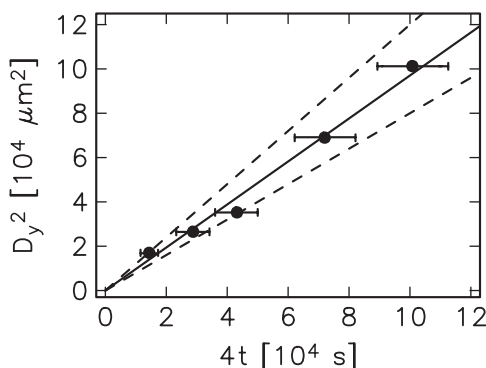


Figure 5. Diffusion depths D_y^2 extracted from the measurements versus quadruple time $4t$. The solid line is a linear fit. The two dashed lines indicate the uncertainty in the determination of the diffusion constant, the horizontal lines represent error bars.

of useful impurity concentration for holography within a few hours of annealing time. This is of great advantage for minimizing surface deterioration of the material resulting from, e.g. lithium outdiffusion during long annealing times. It is also possible to homogeneously dope even volume crystals with a thickness of one or two millimeters by indiffusion of thin evaporated copper layers. For example, a uniform distribution of the copper in our test crystal results in a doping level of $c_{\text{Cu}} = 2000$ mol ppm. This requires an annealing time of 50–100 h which is still acceptable. As a consequence, the photorefractive properties of copper-doped LiNbO₃ volume samples fabricated by the indiffusion method were investigated in [35].

The question remains whether the evaporated copper layer completely diffuses into the substrate. If this holds then the copper concentration can be easily calculated from the thickness of the evaporated layer. Layers of various thickness are evaporated onto 1 mm-thick pieces of y -cut LiNbO₃. After that the samples are annealed for 100 h at 1000°C in air. Then the absolute value of the copper concentration in the crystals is determined with the help of atomic absorption spectrometry. The results are shown as circles in figure 6. Alternatively, the copper concentration can also be calculated from the known thickness of the evaporated layer τ_{Cu} , the molar masses 63.55 g mol^{-1} of copper and $147.85 \text{ g mol}^{-1}$ of LiNbO₃, and the densities of copper (8.93 g cm^{-3}) and LiNbO₃ (4.46 g cm^{-3}). This yields the solid line in figure 6. Obviously, calculation and experimental results fit together very well. This shows that practically all of the copper ions diffuse into the host material. Thus, the precise knowledge of the evaporated layer thickness allows to easily predict the copper concentration in the sample.

4.2. Surface topography: AFM measurements

The surface profiles of some of the fabricated waveguides are investigated with an atomic force microscope (AFM) to get an impression of the quality of the guides after the indiffusion processes. Here, the $8 \mu\text{m}$ -wide channels are scanned along the z -direction. The reconstructed surface topographies extend over an area of $50 \times 50 \mu\text{m}^2$. The results are shown in figure 7 for the waveguide K3 (19 nm Cu) and in figure 8 for the waveguide S4 (83 nm Cu). On the one hand, the surface of

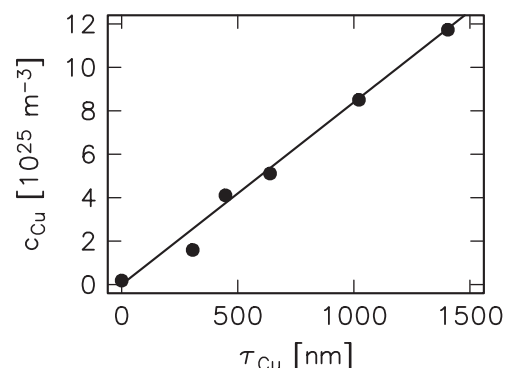


Figure 6. Measured (symbols) and expected (lines) copper content of diffusion-doped LiNbO₃:Cu volume crystals: copper concentration c_{Cu} versus thickness τ_{Cu} of the evaporated copper layer.

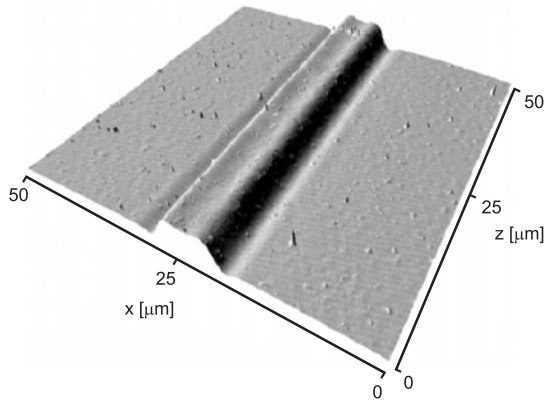


Figure 7. Surface profile of the sample ‘K3’ (19 nm Cu) measured with an AFM. The 8 μm -wide channel is shown.

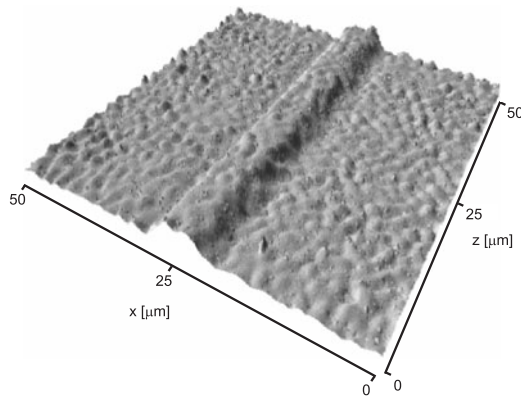


Figure 8. Surface profile of the sample ‘S4’ (83 nm Cu) measured with the AFM. Again the 8 μm -wide channel is shown.

sample K3 looks similar to that of the undoped sample U3 that was used as a reference. Both are flat and smooth. On the other hand, the surface of the strongly copper doped sample S4 is very rough. For all samples we observe that during the indiffusion process the channels expand out of the surface. The generated difference in height between the titanium doped region and the undoped substrate is approximately 200 nm.

4.3. Waveguide losses

Figure 9 shows measurements of the optical density OD_y of some of the prepared samples versus the probe light energy E . Here, the bulk samples are investigated along the y -direction with a free-space spectrometer. In each case, the corresponding curve for an undoped sample, which serves as a reference, has been subtracted to visualize the effect of the indiffused copper. This means that the curves give an impression of the influence of the dopant on the whole substrate material, not on the channel waveguides. The energy of the green light of the argon ion laser at 2.4 eV and the energy of the infrared light emitted by the DFB laser at 0.8 eV are marked on the energy scale. A magnification of 50 times has been used for the left part of the diagram. The measured spectra look very similar to those of conventionally fabricated $\text{LiNbO}_3 : \text{Cu}$ volume crystals doped in the melt: the shoulder starting at approximately 2 eV (620 nm) is induced by the Cu^+ ions, whereas the small band centred around 1.2 eV

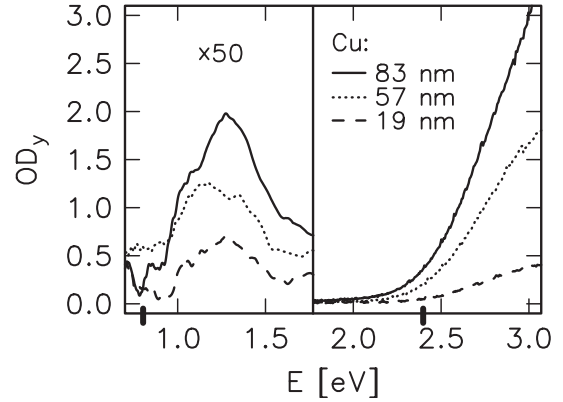


Figure 9. Optical density OD_y of the samples along the y -direction versus wavelength λ of the probe light.

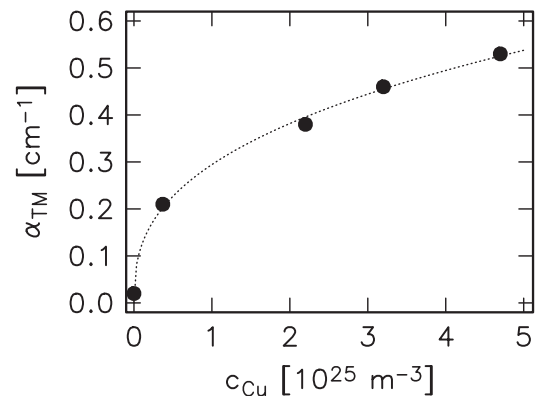


Figure 10. Waveguide losses α_{TM} of 6 μm -wide channels versus copper concentration c_{Cu} . The probe light is TM-polarized and has a wavelength of $\lambda = 1555.4$ nm. The dashed line is a guide for the eye.

(1030 nm) originates from the Cu^{2+} present in the samples. Both characteristics become more pronounced with increasing copper concentration. Especially the shoulder starting at 2 eV rises dramatically. For infrared light around 1550 nm no clear tendency is observed. In this range, we measure $OD_y \leq 0.01$ for all samples. It is not appropriate to calculate absorption spectra $\alpha(E)$ from $OD_y(E)$ because the copper concentration is inhomogeneous along the y -direction. Figure 10 presents direct measurements of the waveguide losses α_{TM} at a wavelength of 1555.4 nm versus the copper concentration c_{Cu} . Here, the 6 μm -wide channels are investigated. In these samples, the copper diffusion was carried out under argon atmosphere, i.e. the samples are slightly reduced. The losses of the waveguides strongly depend on c_{Cu} . The undoped sample investigated for comparison shows by far the lowest loss. Here, a value of $\alpha_{\text{TM}} = 0.02 \text{ cm}^{-1}$ is found, which is equal to a loss of only 0.09 dB cm^{-1} . For the highest doping level $\alpha_{\text{TM}} = 0.53 \text{ cm}^{-1}$ is measured which corresponds to a loss of 2.30 dB cm^{-1} .

Figure 11 shows the waveguide losses for samples with equal copper doping level (38 nm Cu evaporated) but different reduction states of the indiffused copper. One sample (K5) was annealed in the common way under argon atmosphere. Another one (W3) was annealed in oxygen environment. Here, more copper ions have been transferred into the Cu^{2+} state. The third sample was annealed in vacuum atmosphere. In

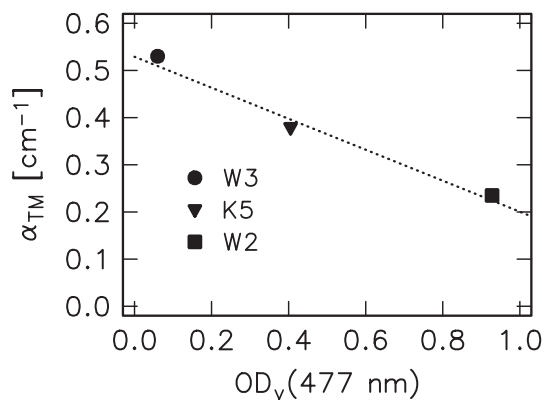


Figure 11. Waveguide losses α_{TM} of samples with the same copper content but different reduction state of the copper versus optical density at 477 nm. The wavelength of the probe light is 1557 nm. The dashed line is a guide for the eye.

this way, more copper ions have been transferred into the Cu^+ state, which means that the sample is reduced more strongly. Consequently, the samples show a different optical density at 477 nm when measured with the free-space spectrometer along the y -axis. Figure 11 shows the light absorption α_{TM} at 1554 nm in the channels versus the optical densities OD_y at 477 nm. It is found that infrared light travelling in the oxidized sample suffers the highest losses, in contrast to the strongly reduced sample which shows the lowest absorption.

4.4. Holographic reflection gratings: filter shapes

Typical results of transmission scans of holograms recorded in the $8\ \mu\text{m}$ -wide channel of waveguide S6 are shown in the figures 12 and 13. Figure 12 shows the channel transmission after a 1.7 mm long grating has been recorded at room temperature for 60 min. The grating reaches a diffraction efficiency of 82% and a bandwidth (FWHM) of 0.48 nm. The solid line is a fit curve according to equation (16) yielding $\Delta n = 4.4 \times 10^{-4}$. For comparison, figure 13 shows the transmission scan of a 16.0 mm-long grating recorded in the same waveguide. This time, recording was performed for 1 min at room temperature. This grating reaches 77% diffraction efficiency and a bandwidth of 0.07 nm. Again, the solid line is a fit curve and yields $\Delta n = 4.7 \times 10^{-5}$.

Both, the experimental and theoretical dependence of the FWHM on the total grating length d for a grating with $\eta = 80\%$ is presented in figure 14. The squares represent data measured with waveguide S6 and the solid line was calculated according to equation (16). Obviously, theory and experiment fit together fairly well.

To demonstrate the multiplexing capabilities of the fabricated channel waveguides three reflection holograms with a peak spacing of 0.8 nm are superimposed in the sample S6. The holograms are recorded one after the other, and the exposure times and recording angles are $t = 16$ min and $2\Theta = 93.87^\circ$ for grating (a), $t = 4$ min and $2\Theta = 93.93^\circ$ for grating (b), $t = 1.5$ min and $2\Theta = 93.99^\circ$ for grating (c). Each grating is 16.0 mm long. The resulting transmission spectrum $T(\lambda)$ of the channel waveguide for the TM mode is plotted in figure 15. For the three gratings diffraction efficiencies of 84.9%, 96.7% and 95.2% are measured, respectively. The

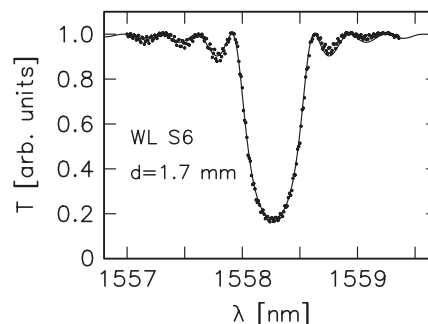


Figure 12. Transmission T as a function of readout wavelength λ for a 1.7 mm long grating recorded in the waveguide S6. The recording time is 60 min at room temperature. The solid line is a fit curve.

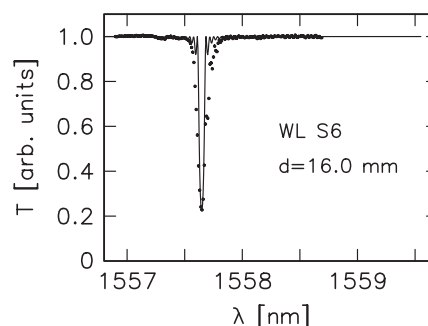


Figure 13. Transmission T as a function of readout wavelength λ for a 16.0 mm long grating recorded in the waveguide S6. The recording time is 1 min at room temperature. The solid line is a fit curve.

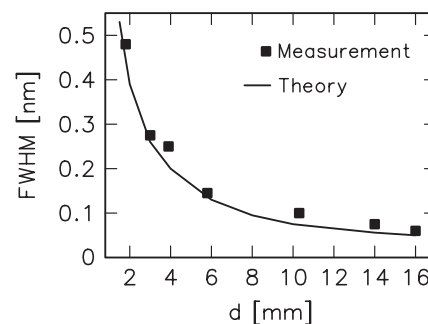


Figure 14. Peak width FWHM of reflection gratings versus grating length d for holograms recorded in waveguide S6 (■) and theoretical values (—).

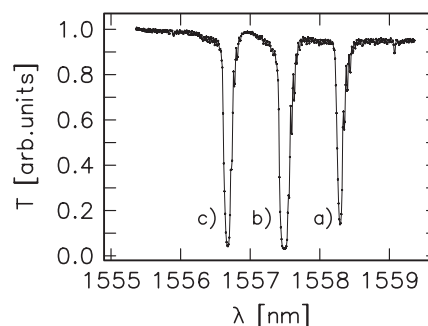


Figure 15. Three superimposed reflection holograms for infrared light in an $8\ \mu\text{m}$ -wide channel in sample S6 (83 nm Cu). The normalized transmission T of the waveguide is shown versus the readout wavelength λ . A hologram spacing of 0.8 nm is realized.

corresponding peak wavelengths λ_p are 1558.29, 1557.50 and 1556.68 nm. An important characteristic of these reflection gratings is the minimum peak width FWHM that can be obtained. Here, the peak widths of the three gratings are 0.12 nm, 0.15 nm and 0.09 nm, respectively.

4.5. Effective refractive indices

The fabrication of an integrated wavelength filter operating at a predefined peak wavelength λ_p requires the knowledge of the effective refractive index n_{eff} of the guided mode in the channel waveguide. Then the appropriate recording angle is given by equations (19) and (20). The measured values n_{eff} for the $8\ \mu\text{m}$ -wide channel waveguides are presented in figure 16 versus the copper concentration c_{Cu} . In each case, the TM mode is excited. A slight increase of n_{eff} is observed for large copper doping levels. The corresponding substrate refractive index is $n_{\text{sub}} = 2.2110$ (see below). The dashed line is a guide for the eye.

4.6. Photorefractive properties

In the next step, the fundamental photorefractive properties of the fabricated waveguides are investigated. Reflection gratings are recorded in various waveguides and read in the $8\ \mu\text{m}$ wide channels with infrared light. Long recording times lead to strong refractive-index changes. For waveguides of typically 16 mm in length, this results in a large uncertainty in the determination of Δn , because the diffraction efficiency of the hologram gets very close to $\eta = 1$. Consequently, for long recording times short gratings are desired and a narrow slit mask is placed on top of the waveguide during recording. This allows to keep the diffraction efficiency of the grating well below $\eta = 1$ and the corresponding refractive-index change can be calculated precisely. Figure 17 shows the results for waveguides with three different copper concentrations but equal argon diffusion atmosphere. The measured refractive-index change Δn versus recording time t is presented, extracted from the filter shapes by fits according to equation (16). Here, the solid lines represent mono-exponential fits following equation (13). The saturation values of Δn , extracted from these fit curves, are shown versus c_{Cu} in figure 18. A linear dependence is observed, indicated by the solid line.

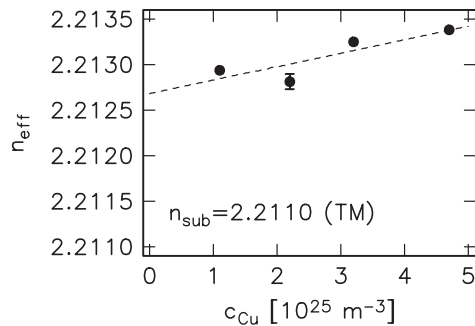


Figure 16. Effective refractive index n_{eff} of the TM mode in an $8\ \mu\text{m}$ -wide channel extracted from the holographic measurements versus copper concentration c_{Cu} in the channels. The dashed line is a linear fit.

The photoconductivity σ_{ph} in the channels is determined by measuring the decay of reflection holograms under homogeneous illumination with green light. Transmission scans are taken from time to time and the corresponding refractive-index modulation is calculated. All curves $\Delta n(t)$ are well fitted by single exponentials according to equation (14). The extracted values σ_{ph} for selected samples are plotted in figure 19 versus the intensity I of the green erasure light in the channels. Each data set is described well by a linear fit: the photoconductivity of $\text{LiNbO}_3:\text{Ti}$ channel waveguides doped by copper indiffusion depends linearly on the light intensity.

4.7. Thermal fixing of holograms

A holographic grating written at room temperature is not stable enough for most applications. The dark conductivity in the

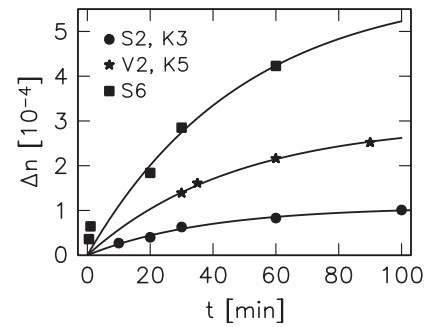


Figure 17. Light-induced refractive-index modulation versus recording time t for selected copper-doped channel waveguides. The curves are mono-exponential fits.

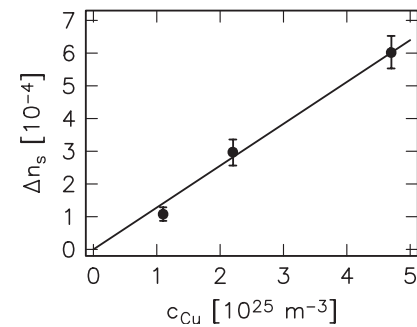


Figure 18. Saturation values Δn_s of the refractive-index modulation induced by the green recording light in the channel waveguides versus copper concentration c_{Cu} . The solid line is a linear fit.

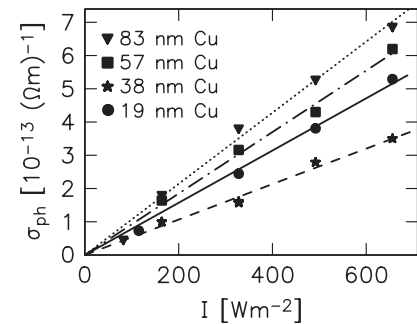


Figure 19. Photoconductivity σ_{ph} of some investigated channel waveguides versus intensity I of the green erasure light. The lines are linear fits.

channel waveguides is not negligible and a slow decay of the diffraction efficiency of a recorded hologram is observed. The decay time observed in our samples with lowest doping level is in the range of 6 month, whereas the decay time for the highest doping level is just a few days. Nevertheless, the technique of thermal fixing yields quasi-permanent holograms.

Thermal fixing works in the fabricated copper-doped LiNbO_3 waveguides, too. First a reflection grating is recorded for 60 min at 180°C in the ‘oxidized’ waveguide W3. After cooling down to room temperature a transmission spectrum $T(\lambda)$ of the $8\ \mu\text{m}$ -wide channel is taken. The result is shown in the upper part of figure 20. At this stage, only a very small Bragg peak is observed. This is the well expected behaviour from the theory of thermal fixing in doped LiNbO_3 volume crystals [36–38]. Now the fixed hologram is revealed by a homogeneous illumination with green light until saturation occurs. The resulting transmission curve $T(\lambda)$ is shown in the bottom part of figure 20. As expected, a strong Bragg peak appears. In this plot, the filter shape already shows a ‘flat top’. From a fit curve according to equation (16) a refractive-index modulation of $\Delta n = 2.0 \times 10^{-4}$ in the channel is deduced.

In a next step the ‘reduced’ waveguide T4 is investigated. In contrast to the sample W3 this sample was annealed in argon atmosphere. Furthermore, the copper concentration in the channel is more than two times higher. A grating is recorded for 120 min at 180°C . Directly after cooling down a transmission spectrum is taken. Figure 21 again shows the result for the $8\ \mu\text{m}$ -wide channel. A strong Bragg peak is identified and the measured diffraction efficiency reaches 96% at a centre wavelength of $\lambda = 1557.81\ \text{nm}$. The filter shape is very sharp and the line width (FWHM) is less than $0.09\ \text{nm}$. It is stressed that until now no development process has been applied to the sample.

Now the fixed grating in the sample T4 is revealed with green light. The measured time evolution of the refractive-index modulation Δn is presented in figure 22. It first drops down rapidly, then passes through a minimum, and finally reaches a steady state after around 5000 s. This saturation value is smaller than the initial value Δn_0 . The solid line is a

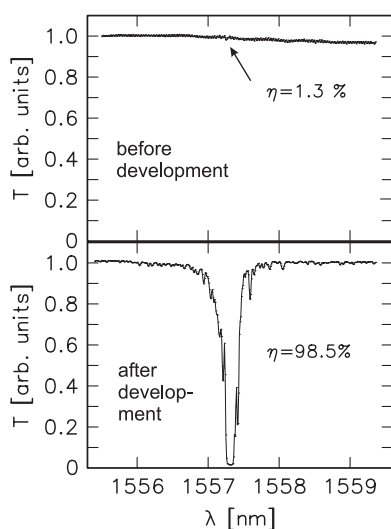


Figure 20. Transmission T before and after the development process versus readout wavelength λ for a grating recorded for 60 min in the oxidized waveguide W3.

fit curve following a simple model presented below. The fact that the refractive-index change after development is smaller than the initial one is exactly the opposite of what one expects from the common theory of thermal fixing.

Finally the developed refractive-index grating is kept at room temperature in the dark and the time evolution of Δn , resulting from the non-negligible dark conductivity in the sample, is monitored over a total time of 250 h. The data is shown in figure 23. Again Δn first decreases, passes through a minimum and grows again until saturation occurs. Now the saturation value is larger than the start value. The solid line is again a fit curve according to the model presented below. It is remarkable that the start and end values practically coincide

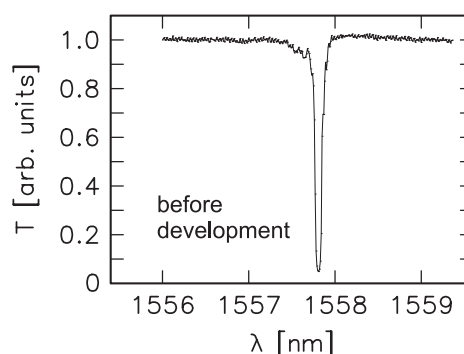


Figure 21. Transmission T versus readout wavelength λ for a grating recorded for 120 min in the reduced waveguide T4 before the development process.

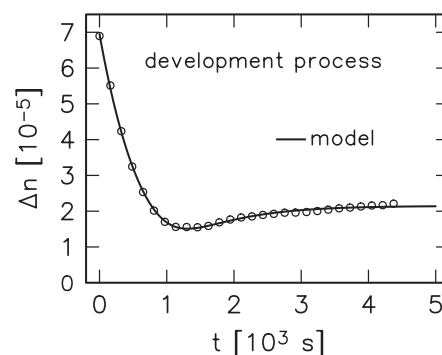


Figure 22. Time evolution of the refractive-index modulation Δn during the development of the fixed grating in waveguide T4. The solid line is a fit according to equation (25).

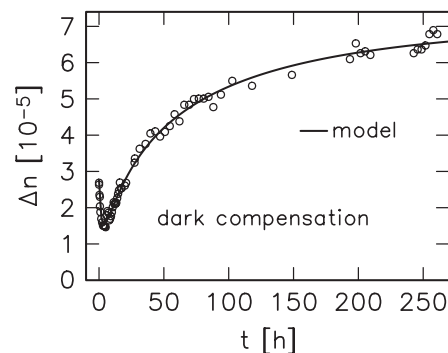


Figure 23. Time evolution of the refractive-index modulation Δn in the dark for the grating in waveguide T4. The solid line is a fit according to equation (26).

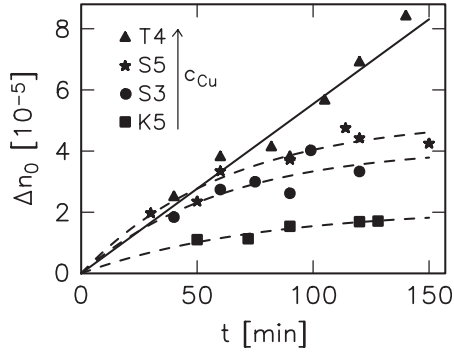


Figure 24. Permanent refractive-index modulations Δn_0 obtained without development versus recording time t for the investigated reduced channel waveguides. The lines are guides for the eye.

with those obtained from the development process: when the revealed grating is kept in the dark Δn evolves back to its initial value before the development process. In the dark the initial value Δn_0 is stable: after more than one year we checked the filter shape of an undeveloped grating with $\eta = 90\%$ in the sample S5 and found no measurable decay of the diffraction efficiency. This effect has not been described in literature so far and is extremely interesting for long-term holographic storage.

The presented time evolution of Δn either under homogeneous illumination and in the dark is similar for all ‘reduced’ waveguides that are investigated. Directly after recording a pronounced refractive-index modulation is already found in the channels, resulting in a strong Bragg peak for the infrared probe light. When the sample is kept long enough in the dark after development of the grating it tends to restore its initial value measured directly after recording. Figure 24 shows these initial refractive-index modulations Δn_0 for the investigated ‘reduced’ waveguides versus the recording time t . The values grow with the recording time and with the copper concentration in the channels. The data for the samples K5, S3, and S5 are well fitted by single exponentials with a time constant around 60 min (dashed lines in figure 24). The values obtained with the sample T4, which has the strongest dopant concentration, still grow almost linearly over the investigated time interval (solid line).

4.8. Switching of Bragg gratings utilizing external electric fields

In the following, we investigate polarization tuning and electrical switching of the fabricated filters by applying external electric fields. A reflection grating is recorded at room temperature in the waveguide X1-5. The recording time is 2 min. The sample is mounted into the readout setup and a transmission scan is performed. A strong Bragg peak appears, the diffraction efficiency for the infrared light reaches 97.6%. However, the centre wavelength λ_p of the reflection hologram depends on the polarization state of the readout light: for the TE mode λ_p it is about 0.1 nm larger than for the TM mode. This is a disadvantage for many applications in telecommunication because optical fibre networks use unpolarized light. Obviously, the goal is to let the integrated component work polarization independently, too. Here, electro-optic materials offer a unique opportunity: with

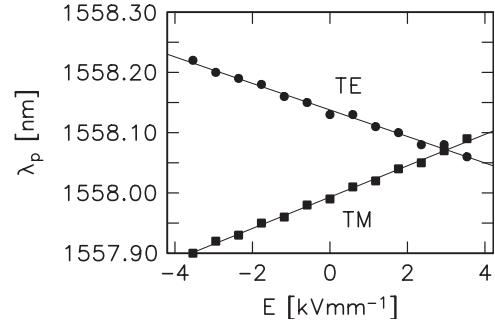


Figure 25. Centre wavelength λ for the TE and the TM mode versus external electric field E . The solid lines are linear fits.

the use of external electric fields, the refractive index of the material, and thus the propagation constant of the guided mode, can be increased or decreased, depending on the sign of the applied electric field. This allows to tune the centre wavelength of the recorded hologram to a larger or smaller value.

For this purpose, plane parallel electrodes are deposited on the waveguide X1-5 next to the $6\ \mu\text{m}$ -wide channel. The electrodes are contacted and a constant voltage is applied. For various voltages transmission scans of the channel are performed, both with the TE and the TM mode. Figure 25 shows the extracted centre wavelength λ_p versus the external electric field E in the channel, calculated according to equation (23). We find that λ_p depends linearly on E . The shift for the TE mode is opposite to the shift for the TM mode. Consequently, there exists a defined value of E where the centre wavelengths for the TE and the TM mode coincide, thus realizing a filter that works polarization independently. In our experiment this occurs when a field of $3\ \text{kV}\ \text{mm}^{-1}$ strength is applied to the channel waveguide.

4.9. Thermal tuning of Bragg gratings

Fine tuning of the centre wavelength of a Bragg grating in a channel waveguide is also possible by adjusting the temperature of the unit. For example, devices for telecommunication often use thermoelectric coolers to control their temperature and keep their parameters in specification. However, the speed of thermal tuning is low and cannot be compared to that of tuning via the electro-optic effect. To measure the response of a grating in a LiNbO_3 channel waveguide on the temperature of the environment, a 16 mm-long waveguide with a thermally-fixed Bragg grating is connected permanently with an input and an output optical fibre [39]. The fibres are glued to the LiNbO_3 substrate with an ultraviolet sensitive adhesive after adjusting them to the correct position with a piezo-controlled xyz translation stage. Then the device is placed into a small oven precisely controlled by a PID controller. The temperature is adjusted carefully to different values, and after a sufficiently long waiting time a transmission scan of the device is performed. Figure 26 shows the resulting centre wavelength λ_p for the TM mode as a function of the temperature T . Over the investigated temperature interval from 295 to 328 K a linear dependence is observed. From a linear fit the tuning coefficient α for the temperature response of the device is calculated:

$$\alpha_3 = (4.5 \pm 0.5) \times 10^{-6}\ \text{K}^{-1}.$$

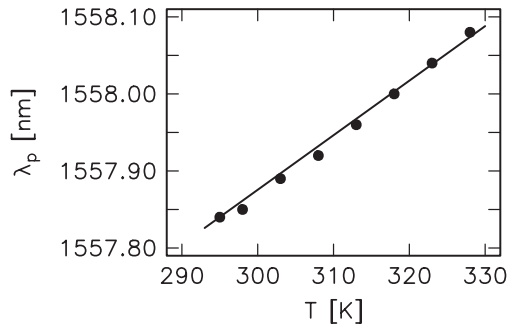


Figure 26. Centre wavelength λ_p for the TM mode versus temperature T . The solid line is a linear fit.

Here, the subscript 3 means the thermal response along the c -axis of the LiNbO₃ substrate. With this value the centre wavelength can be derived according to the relation $\lambda = \lambda_0(1 + \alpha_3 \Delta T)$, with ΔT as the corresponding temperature difference and λ_0 as the starting centre wavelength.

5. Discussion

5.1. Waveguide losses and optical density

The increased losses of the copper doped channel waveguides around 1550 nm are caused by two effects. Figures 7 and 8 indicate that the surface roughness rises strongly for high copper doping levels in the channels. This may originate from an increased outdiffusion of lithium ions [40] during the indiffusion of thick layers of copper. As a result, for highly doped samples light gets lost due to strong scattering through the channel surface. As a second effect, absorption of the infrared light in the channel resulting from the presence of Cu²⁺ has to be taken into account, too. The absorption band around 1.1 μm still extends to 1.55 μm. This is indicated by the strong increase of the waveguide loss α_{TM} already for a low copper doping level, as shown in figure 10.

There is substantial hope that the losses of the waveguides can be significantly decreased if the copper indiffusion is performed in a highly reducing environment, e.g. in vacuum atmosphere. This lowers the number of Cu²⁺ centres in the channels and consequently the absorption band at 1.1 μm. This effect already shows up in figure 11, where the losses for samples with different reduction state of the copper ions but equal total copper concentration are investigated. The oxidized sample has the smallest Cu⁺ content, thus it shows the lowest optical density in the visible at 477 nm. However, it has the largest Cu²⁺ content, so its absorption in the infrared at 1.55 μm is maximal. For the sample W3 the situation is vice versa. This can be easily understood because it was indiffused in vacuum atmosphere, which turns more copper ions into the reduced Cu⁺ state, thus lowering the number of Cu²⁺ centres.

5.2. Holographic measurements

Figure 16 shows that the effective refractive indices n_{eff} of the TM mode in the investigated 8 μm-wide channel waveguides range from 2.2127 to 2.2134. Obviously, the refractive index of the substrate material must be below these values. An interpolation of data from [41] yields the ordinary refractive

index of undoped LiNbO₃ at 1557 nm, which is $n_0 = 2.2110$. This means that the refractive-index increase for the TM mode induced by the indiffused titanium is about 2×10^{-3} .

An additional small increase of n_{eff} appears for large copper doping levels. As c_{Cu} is practically constant in the channels (figure 2) this suggests that the indiffused copper slightly enhances the refractive index n_0 of the substrate. However, this increase induced by the presence of copper is very small compared to the influence of the indiffused titanium. It may already be in a range where an unavoidable tolerance during waveguide fabrication can significantly affect the experimental results.

As a further test, the intensity distribution at the rear endface of the channel waveguides is imaged onto an infrared camera system to check if the indiffused copper induces an additional planar waveguide at the surface of the doped region of the samples. However, this is not the case. Even for the highest copper doping level no guided light is observed next to the titanium-indiffused channels. This holds for both polarization states of the infrared light.

According to figure 19 the photoconductivity of the investigated waveguides rises linearly with the light intensity. The same dependence is predicted by the one-centre model. Thus, only the copper ions are responsible for the photorefractive effect in the waveguides, an influence of the titanium ions defining the channels is not observed. No obvious relation between the slope $\sigma_{ph,0} \equiv \sigma_{ph}/I$ and c_{Cu} is observed. The values for $\sigma_{ph,0}$ extend from 5.3×10^{-16} to 10.7×10^{-16} m V⁻². This is in fairly good agreement with data obtained for homogeneously doped volume crystals containing roughly the same amount of copper [35].

The second prediction of the one-centre model, $\Delta n_s \propto c_{Cu^{2+}}$, cannot be checked directly because the total Cu²⁺ content in the channels is unknown. If we assume that the reduction state $c_{Cu^+}/c_{Cu^{2+}}$ only slightly differs from sample to sample, which can be justified by the equal annealing treatment of all waveguides, Δn_s should also increase linearly with the total copper concentration c_{Cu} . This linear dependence is observed in figure 18. The maximum values of Δn_s coincide with those of highly copper- or iron-doped LiNbO₃ volume crystals [35, 42]. This means that the indiffused titanium ions do not lead to any significant decrease of the achievable light-induced refractive-index change.

For applications like wavelength filtering a high diffraction efficiency is required. From equation (18) one obtains that a refractive-index modulation of $\Delta n = 1.3 \times 10^{-4}$ yields a theoretical diffraction efficiency of $\eta = 99.9\%$ for a 16 mm-long grating. This is equal to a rejection ratio of 30 dB for the peak wavelength λ_p . Figure 18 shows that this can already be realized with a moderate copper doping level. If a substantial data stream, e.g. on a 2.5 or 10 Gbit⁻¹ transmission system, is to be passed through the filter, a filter shape following a ‘flat top’ function is desired. This behaviour is observed for the strong grating fixed in the waveguide W3, shown in figure 20.

5.3. Model for thermal fixing

To explain the observed time evolution of the refractive-index modulation of thermally fixed gratings in the ‘reduced’

samples, either under homogeneous illumination or in the dark, it is assumed that the measured values for Δn result from a superposition of two different refractive-index gratings, Δn_c and Δn_b , that are simultaneously present in the waveguides [43]. The two gratings are nearly 180° out of phase. The small angle mismatch to 180° is labelled φ . The first grating, Δn_c , grows already during the high temperature recording and remains constant after the sample has cooled down again. At room temperature this grating is insensitive to photoactive light. In particular, this means that even the revealing light shining on the sample does not change Δn_c . In contrast, the second grating Δn_b is just generated during the development process. While the sample is illuminated homogeneously, Δn_b grows exponentially with a time constant τ_1 until saturation. From this model the time evolution for the development process is derived:

$$\Delta n(t) = \left\{ \left[\Delta n_c - \Delta n_b^0 \cos \varphi \left(1 - \exp \left(-\frac{t}{\tau_1} \right) \right) \right]^2 + \left[\Delta n_b^0 \sin \varphi \left(1 - \exp \left(-\frac{t}{\tau_1} \right) \right) \right]^2 \right\}^{1/2}. \quad (25)$$

The solid line in figure 22 is a corresponding fit to the measured data, which yields

$$\Delta n_c = 7.0 \times 10^{-5}, \quad \Delta n_b^0 = 8.3 \times 10^{-5}, \\ \varphi = 12.6^\circ \quad \text{and} \quad \tau_1 = 770 \text{ s}.$$

To describe the dark evolution of Δn after the development process it is assumed that the grating Δn_b is erased according to a stretched exponential function, whereas the grating Δn_c remains again constant. The model predicts a time evolution in the dark following the relation:

$$\Delta n(t) = \left\{ \left[\Delta n_c - \Delta n_b^0 \cos \varphi \exp \left(-\left(\frac{t}{\tau_2} \right)^\gamma \right) \right]^2 + \left[\Delta n_b^0 \sin \varphi \exp \left(-\left(\frac{t}{\tau_2} \right)^\gamma \right) \right]^2 \right\}^{1/2}. \quad (26)$$

The corresponding fit is shown in figure 23 as a solid line. For $\gamma = 1$ (mono-exponential decay) a convincing fit to the measured data is impossible. The best coincidence is found with the parameters $\Delta n_c = 7.0 \times 10^{-5}$, $\Delta n_b^0 = 9.3 \times 10^{-5}$, $\varphi = 12.4^\circ$, $\tau_2 = 37.7 \text{ h}$ and $\gamma = 0.53$. The values for Δn_c , Δn_b^0 and φ agree very well to those found for the development process.

The time evolution of the grating Δn_b can be well explained as that of a photovoltaic grating. In LiNbO_3 crystals the photovoltaic effect is the main charge driving force. During the fixing process a deep modulation of the Cu^+ traps arises because the space charge field is permanently compensated by screening ions that are mobile at high temperatures [26]. After cooling down the homogeneous illumination generates modulated photocurrents resulting from the deep modulation of the Cu^+ traps. Now a space charge field builds up that modulates the refractive index via the electro-optic effect and the grating Δn_b appears.

After the development process the photovoltaic grating Δn_b is slowly erased via the dark conductivity of the material. Recently, the dark erasure of holograms recorded

in $\text{LiNbO}_3 : \text{Fe}$ at room temperature has been found to follow a stretched exponential function [44]. This is the same type of function used for the model describing the dark compensation.

The permanent grating Δn_c is most likely attributed to the copper ions in the samples. This conclusion is based on the fact that the measured permanent gratings Δn_c are uniquely found in $\text{LiNbO}_3 : \text{Cu}$ and not in $\text{LiNbO}_3 : \text{Fe}$ crystals. If the grating Δn_c was formed by a deep modulation of protons during the fixing process it should also be present in $\text{LiNbO}_3 : \text{Fe}$, which is not the case. There are two possibilities for the copper ions to generate the grating Δn_c . First the deep modulation of Cu^+ and Cu^{2+} can already lead to material changes that cause a measurable sinusoidal refractive-index change in the samples. If enough ions are present for charge compensation, the modulation degree of Cu^+ can reach almost a value of one. Furthermore, it is not established that protons, like in $\text{LiNbO}_3 : \text{Fe}$, are responsible for the compensation of the space charge field during thermal fixing in $\text{LiNbO}_3 : \text{Cu}$. The diffusion constant of copper in LiNbO_3 is nearly 500 times larger than that of iron under the same conditions. Furthermore, in our experiments the period of the recorded Bragg gratings is only about 350 nm. Therefore, the distance the compensating ions have to move during the high temperature recording is relatively small. If one takes into account that during thermal fixing the ions also drift in a strong space charge field it might be possible that the Cu^{2+} ions themselves, and not only protons, act as the compensating ions. This means that the copper concentration itself is modulated during thermal fixing, not only the distribution of the Cu^+ and the Cu^{2+} ions.

It can be ruled out that Δn_c results from an absorption grating formed during the recording process. Cu^{2+} introduces an absorption band around $1.1 \mu\text{m}$ in LiNbO_3 and it might be argued that an absorption grating for the infrared light is formed. The absolute diffraction efficiency η_{abs} of a reflection grating of this kind, taking into account absorption losses in the sample, is limited to 7.2% [24]. Here, η_{abs} is defined as the ratio I_d/I_r , where I_d is the intensity of the diffracted beam and I_r the intensity of the readout beam impinging on the sample. From a direct measurement with an undeveloped reflection grating thermally-fixed for 140 min in the sample T4 we find a far higher value of $\eta_{\text{abs}} = (55 \pm 10)\%$.

In the next step the phase shift between the two gratings is discussed. During homogeneous illumination electrons are excited from Cu^+ ions into the conduction band. In doped LiNbO_3 the drift length for electrons is small. Therefore the charge distribution ρ originating from trapped electrons has a phase shift of 90° to the Cu^+ distribution. The resulting space charge field is deduced from Maxwell's equation $\text{div E} = \rho/\epsilon\epsilon_0$. This introduces again a phase shift of 90° for the developed space charge field and consequently for the grating Δn_b . Finally, this means that Δn_b and the Cu^+ distribution have a phase shift of 180° .

If the grating Δn_c results from material changes caused by a redistribution of the copper ions it can be either in phase or counter phase to the Cu^+ distribution. Assuming that it is in phase this fits to the model very well. This means that Δn_b and Δn_c ideally have a phase shift of 180° , equivalent to $\varphi = 0$ in our model. From the measurement we find that the angle φ is not exactly zero. This can be understood if one takes

into account that for the small grating periods of about 350 nm a diffusion grating can not in any case be neglected versus the strong photovoltaic grating. From the relations $E_{\text{diff}} = k_B T K / e$ [45, 46] and $\Delta n_{\text{diff}} = -0.5 n^3 r E_{\text{diff}}$ a maximum strength of $\Delta n_{\text{diff}} = 1.7 \times 10^{-5}$ is calculated for the diffusion grating. Here, T is the temperature, $K = 2\pi/\Lambda$ the spatial frequency, n the refractive index and r the appropriate element of the electro-optic tensor. In LiNbO₃ the diffusion and the photovoltaic grating have a phase shift of 90° [45, 46]. Thus, if Δn_{diff} participates in Δn_b , it induces the small phase shift $\varphi \neq 0$.

5.4. Electric fields: switching of gratings and electro-optic coefficient

From the above experiments with applied external electric fields it is found that the centre wavelength λ_p of a recorded reflection grating can be tuned by adjusting the applied voltage. Hereby, the centre wavelength for the TE mode and the TM mode is shifted in the opposite direction and there exists a point where they both coincide. Consequently, the applied electric field allows to switch the grating ‘on’ or ‘off’ for a specific wavelength of the infrared light. Modern telecommunication networks use a set of, e.g. 40 channels between 1520 and 1570 nm that are separated by gaps of 100 GHz, which is about 0.8 nm. Furthermore, there is a tendency to move towards 50 GHz or even 25 GHz systems. Switching a Bragg grating to the ‘on’ state means that the field E is properly selected to match λ_p for the TE and the TM mode on a predefined wavelength channel. On the other hand, the ‘off’ state uses a value of E that switches λ_p for the TE mode to one side next to the wavelength channel, and for the TM mode to the other side. So the grating is ‘hidden’ for the WDM network because none of its channels fulfills the Bragg condition. As a consequence, all wavelength channels pass the device unaffected. The switching speed of such a device can be extremely fast, because the electro-optic effect follows the applied electric field instantaneously.

Furthermore, the experimental results presented in figure 25 allow to calculate the magnitude of the involved linear electro-optic coefficient in the channel waveguide. In this special experiment, we use channels directed along the z -axis in an x -cut LiNbO₃ sample. The electrodes are deposited on the top side, parallel to the channel waveguide. Thus, we deal with an electric field E_2 along the y -direction. The light polarization can be either TM, which means polarized along the x -direction, or TE, which means polarized along the y -direction. Consequently, the involved elements of the linear electro-optic tensor are r_{12} for TM and r_{22} for TE. The symmetry of the electro-optic tensor r_{ijk} requires $r_{12} = -r_{22}$. This is the reason why the centre wavelength for the TE and the TM mode are shifted in the opposite direction when a field is applied. With the help of equation (22) the results from figure 25 allow to calculate r_{12} and r_{22} in the channel waveguide. The linear fits, together with the known grating period Λ and the known effective refractive indices for the TE and the TM mode yield $r_{12} = (6.8 \pm 0.7) \text{ pm V}^{-1}$ and $r_{22} = -(5.8 \pm 1.5) \text{ pm V}^{-1}$. The literature values for LiNbO₃ bulk crystals are $r_{12} = -r_{22} = 6.8 \text{ pm V}^{-1}$ [47]. This coincides with our value very well.

6. Conclusions

In summary, this work reports on the investigation of photorefractive single mode channel waveguides in LiNbO₃ fabricated by titanium- and additional copper-indiffusion. The waveguide losses for infrared light around 1.55 μm strongly depend on the copper impurity level and the reduction state of the copper ions. The fundamental photorefractive properties of the waveguides are similar to those of conventionally doped LiNbO₃:Cu volume crystals and in accordance with the predictions of a one-centre model for the charge transport. Guided infrared light is efficiently diffracted from reflection gratings recorded with green light of an argon ion laser. With the help of an applied electric field, this allows to fabricate polarization insensitive, fast switchable filters. Such a switchable filter in an add/drop geometry that uses a bi-modal waveguide section and directional coupler, together with a slanted refractive-index grating that couples the first two modes of the waveguide, is currently under investigation in our laboratory.

Thermal fixing is investigated in detail in the fabricated waveguides. Strong refractive-index modulations, most likely not originating from the photorefractive effect but from permanent material changes, arise without the need of any development process after the fixing procedure. Such gratings show no measurable decrease of their diffraction efficiency for at least one year. The maximum obtained refractive-index modulation grows with the copper doping level and reaches 1×10^{-4} for a strongly doped sample. This new effect is potentially attractive for long-term holographic storage.

Acknowledgments

Financial support of the Deutsche Forschungsgemeinschaft (Sonderforschungsbereich 225 at University of Osnabrück, Germany, Teilprojekt D9 and grant KI482/6-1) is gratefully acknowledged.

References

- [1] Tamir T (ed) 1990 *Guided-wave Optoelectronics* (Heidelberg, Berlin: Springer)
- [2] Prokhorov A M, Kuzminov Y S and Khachatryan O A 1996 *Ferroelectric Thin-Film Waveguides in Integrated Optics* (Cambridge: Cambridge International Science)
- [3] Schmidt R V and Kaminov I P 1974 Metal-diffused optical waveguides in LiNbO₃ *Appl. Phys. Lett.* **25** 458–60
- [4] Jackel J L, Rice C E and Veselka J J 1983 Proton exchange in LiNbO₃ *Ferroelectrics* **50** 165–70
- [5] Alferness R C, Schmidt R V and Turner E H 1979 Characteristics of Ti-diffused lithium niobate optical directional couplers *Appl. Opt.* **18** 4012–16
- [6] Burns W K, Lee A B and Milton A F 1976 Active branching waveguide modulator *Appl. Phys. Lett.* **29** 790–2
- [7] Becker C, Greiner A, Oesselke T, Pape A, Sohler W and Suche H 1998 Integrated optical Ti:Er:LiNbO₃ distributed Bragg reflector laser with a fixed photorefractive grating *Opt. Lett.* **15** 1194–6
- [8] Zhang D, Ding G and Chen C 1998 Theoretical analysis of guided mode and effective refractive index at 1.53 μm in Ti:LiNbO₃ strip waveguides *J. Lightwave Technol.* **16** 459–64
- [9] Chen F S, LaMacchia J T and Fraser D B 1968 Holographic storage in lithium niobate *Appl. Phys. Lett.* **13** 223–5

- [10] Ashkin A, Boyd G D, Dziedzic J M, Smith R G, Ballman A A, Levinstein J J and Nassau K 1966 Optically-induced refractive index inhomogeneities in LiNbO_3 and LiTaO_3 *Appl. Phys. Lett.* **9** 72–4
- [11] Krätzig E and Orłowski R 1980 Light induced charge transport in doped LiNbO_3 and LiTaO_3 *Ferroelectrics* **27** 241–4
- [12] Popov V L and Shandarov V M 1991 Study of planar waveguides fabricated from lithium niobate by successive diffusion of titanium and copper *Sov. Phys. Tech. Phys.* **36** 1380–2
- [13] Mikami O 1976 Electro-optic light modulation with holographic gratings stored in a Cu-diffused LiNbO_3 plate *Opt. Commun.* **19** 42–4
- [14] Bozhevolya S I, Zolotov E M, Kiselev V A and Sherbakov E A 1979 Investigation of diffraction gratings induced in LiNbO_3 for integrated-optics applications *Sov. J. Quantum Electron.* **9** 216–18
- [15] Hocker G B and Burns W K 1977 Mode dispersion in diffused channel waveguides by the effective index method *Appl. Opt.* **16** 113–18
- [16] Korotky S K, Minford W J, Buhl L L, Divino M D and Alferness R C 1982 Mode size and method for estimating the propagation constant of single-mode Ti : LiNbO_3 strip waveguides *IEEE J. Quantum Electron.* QE **18** 1796–801
- [17] Vollmer J, Nisius J P, Hertel P and Krätzig E 1983 Refractive index profiles of LiNbO_3 :Ti waveguides *Appl. Phys. A* **32** 125–7
- [18] Strake E, Bava G P and Montrosset I 1988 Guided modes of Ti- LiNbO_3 channel waveguides: a novel quasi-analytical technique in comparison with the scalar finite-element method *J. Lightwave Tech.* **6** 1126–35
- [19] Peterson G E, Glass A M and Negran T J 1971 Control of the susceptibility of lithium niobate to laser-induced refractive index change *Appl. Phys. Lett.* **19** 130–2
- [20] Phillips W, Amodei J J and Staebler D L 1972 Optical and holographic properties of transition metal doped lithium niobate *RCA Rev.* **33** 95–109
- [21] Kurz H, Krätzig E, Keune W, Engelmann H, Gonser U, Dischler B and Rüber A 1977 Photorefractive centers in LiNbO_3 studied by optical-, Mössbauer-, and EPR-methods *Appl. Phys.* **12** 355–68
- [22] Glass A M, von der Linde D and Negran T J 1974 High-voltage bulk photovoltaic effect and the photorefractive process in LiNbO_3 *Appl. Phys. Lett.* **25** 233–5
- [23] Mansingh A and Dhar A 1985 The AC conductivity and dielectric constant of lithium niobate single crystals *J. Phys. D: Appl. Phys.* **18** 2059–71
- [24] Kogelnik H 1969 Coupled wave theory for thick hologram gratings *Bell Syst. Tech. J.* **48** 2909–47
- [25] Amodei J J and Staebler D L 1971 Holographic pattern fixing in electro-optic crystals *Appl. Phys. Lett.* **18** 540–4
- [26] Buse K, Breer S, Peithmann K, Kapphan S, Gao M and Krätzig E 1997 Origin of thermal fixing in photorefractive LiNbO_3 crystals *Phys. Rev. B* **56** 1225–35
- [27] An X, Psaltis D and Burr G W 1999 Thermal fixing of 10000 holograms in LiNbO_3 : Fe *Appl. Opt.* **38** 386–93
- [28] Leyva V, Rakuljic G A and O'Conner B 1994 Narrow bandwidth volume holographic optical filter operating at the Kr transition at 1547.82 nm *Appl. Phys. Lett.* **65** 1079–81
- [29] Müller R, Santos M T, Arizmendi L and Cabrera J M 1994 A narrow-band interference filter with photorefractive LiNbO_3 *J. Phys. D: Appl. Phys.* **27** 241–6
- [30] Müller R, Alvarez-Bravo J V, Arizmendi L and Cabrera J M 1994 Tuning of photorefractive interference filters in LiNbO_3 *J. Phys. D: Appl. Phys.* **27** 1628–32
- [31] Hukriede J, Kip D and Krätzig E 1999 Copper diffusion into lithium niobate *Phys. Status Solidi a* **172** R3
- [32] Kip D, Gather B, Bendig H and Krätzig E 1993 Concentration and refractive index profiles of titanium- and iron-diffused planar LiNbO_3 waveguides *Phys. Status Solidi a* **139** 241–8
- [33] Freschi A A and Frejlich J 1995 Adjustable phase control in stabilized interferometry *Opt. Lett.* **20** 635–7
- [34] Hukriede J, Kip D and Krätzig E 2000 Investigation of titanium- and copper-indiffused channel waveguides in lithium niobate and their application as holographic filters for infrared light *J. Opt. A: Pure Appl. Opt.* **2** 481–7
- [35] Peithmann K, Hukriede J, Buse K and Krätzig E 2000 Photorefractive properties of lithium niobate volume crystals doped by copper diffusion *Phys. Rev. B* **61** 4615–20
- [36] Hertel P, Ringhofer K H and Sommerfeldt R 1987 Theory of thermal fixing and application to LiNbO_3 : Cu *Phys. Status Solidi a* **104** 855–62
- [37] Carrascosa M and Agullo-Lopez F 1990 Theoretical modeling of the fixing and developing of holographic gratings in LiNbO_3 *J. Opt. Soc. Am. B* **7** 2317–22
- [38] Yariv A and Orlov S 1995 Holographic fixing, readout, and storage dynamics in photorefractive materials *Opt. Lett.* **20** 1334–6
- [39] Hukriede J, Kip D and Krätzig E 1999 Thermal tuning of a fixed Bragg grating for IR light fabricated in a LiNbO_3 : Ti channel waveguide *Appl. Phys. B* **68** 73–5
- [40] Kaminow I P and Carruthers J R 1973 Optical waveguiding layers in LiNbO_3 and LiTaO_3 *Appl. Phys. Lett.* **22** 326–8
- [41] Nelson D F and Mikulyak R M 1974 Refractive indices of congruently melting lithium niobate *J. Appl. Phys.* **45** 3688–9
- [42] Peithmann K, Wiebrock A and Buse K 1999 Photorefractive properties of highly doped lithium niobate crystals in the visible and near-infrared *Appl. Phys. B* **68** 777–84
- [43] Hukriede J, Kip D and Krätzig E 2001 Permanent narrow-band reflection holograms for infrared light recorded in LiNbO_3 : Ti : Cu channel waveguides *Appl. Phys. B* **72** 749–53
- [44] Nee I, Müller M, Buse K and Krätzig E 2000 Role of iron in lithium niobate crystals for the dark-storage time of holograms *J. Appl. Phys.* **88** 4282
- [45] Kukhtarev N V 1976 Kinetics of hologram recording and erasure in electrooptic crystals *Sov. Tech. Phys. Lett.* **2** 438
- [46] Kukhtarev N V, Markov V B, Odoulov S G, Soskin M S and Vinetskii V L 1979 Holographic storage in electrooptic crystals *Ferroelectrics* **22** 949
- [47] Weis R S and Gaylord T K 1985 Lithium niobate: summary of physical properties and crystal structure *Appl. Phys. A* **37** 191–203